On the isotopic composition of fission fragments

C. Schmitt [a,*], P. Möller [b]

[a] *Institut Pluridisciplinaire Hubert Curien (IPHC), Rue du Loess, 67000 Strasbourg, France*
[b] *P. Moller Scientific Computing and Graphics, P.O. Box 75009, Honolulu, HI 96836-0009, USA*

A R T I C L E   I N F O

A B S T R A C T

We use a newly developed method, based on the original Brownian shape motion (BSM) model, to calculate fission-fragment isotopic yields $Y(Z, N)$. Recent measurements of post-neutron isotopic distributions with better than 1 u resolution make it possible, for the first time, to test in detail this model. We here report on the comparison between the measured and the calculated fission-fragment average neutron number $< N >$ as a function of proton number, as well as isotopic distributions for selected proton numbers. The calculated primary yields are corrected for post-scission neutron evaporation by the fragments. The highly variable dependence of $< N >$ with Z seen in the measurements is also present in the calculations.

1. Introduction

The last two decades or so have seen considerable experimental and theoretical progress in studies of fission. A major experimental breakthrough was the measurement in 1997 at GSI/FRS of fission-fragment charge distributions for 70 different fissioning systems, see for example Refs. [1–3]. A few years later a substantial advance in the modeling of fission potential-energy surfaces was the use of the macroscopic-microscopic method to calculate the nuclear potential energy as a function of five independent shape degrees of freedom. Because 15 to 45 different values of each independent shape coordinate are needed to obtain sufficient accuracy, the potential energy has to be calculated for millions of different nuclear shapes. The structures in calculated fission-fragment yields are directly related to the structures present in the calculated potential-energy surfaces. Therefore, to benchmark the potential-energy-model results detailed comparisons of calculated properties to experimental data were carried out. Some examples of such data are fission-barrier heights, bimodal fission data, spontaneous fission data and superheavy element properties. Details of the method and comparisons to these types of data are in Refs. [4–8].

A quantitative theoretical method that allowed fission-fragment mass yields $Y(A)$ to be calculated for any system and at any energy above the barrier, the Brownian shape motion (BSM) method, implemented a random walk on the previously calculated potential-energy surfaces [9]. The potential-energy model was recently generalized so that potential-energy surfaces with odd-even effects and different N/Z ratios in the two emerging fission fragments can be calculated. These theoretical developments are discussed in Ref. [10]. Because experimental data for $< N > /Z$ were not available at this time, only the calculated odd-even staggering features were compared to readily available experimental charge yields with better than one-Z resolution. However, a very detailed discussion and specification of the full model for $Y(Z, N)$ was given.

A brief summary of the main model features is given in the next section. Theoretical studies of fission-fragment properties is currently a very active field, as reviewed in for example Ref. [11]. However, none of those studies, except those within the semi-empirical GEF approach [12], have looked at $< N > /Z$ ratios and isotopic distributions, which is our focus here. Studies of the detailed neutron and proton composition of fission fragments permit us to investigate in detail the interplay between the various mechanisms that influence the fission process, see e.g. Refs. [13,14]. Such a realistic modeling of isotopic yields is crucial for calculations in astrophysics, as well as for various societal applications.

2. Outline of main model features

In our approach the calculation of fission yields consists of two steps:

1. Calculation of the potential-energy of a nucleus as a function of a set of selected shapes. This set should include all shapes that may be involved in the shape evolution from the ground state to scission.
2. A random walk on these surfaces which allows the calculation of fission-fragment yields.

* Corresponding author.
E-mail address: christelle.schmitt@iphc.cnrs.fr (C. Schmitt).

2.1. Macroscopic-microscopic potential-energy surfaces

To obtain the energy for a specific shape the surface of the shape is defined in a suitable shape parameterization, in our case the three-quadratic surface parameterization [15]. A macroscopic "liquid-drop"-type potential energy is then calculated, the specific model here is given in Ref. [16]. Such a macroscopic model was of enormous importance, despite its simplicity, because it led to the understanding of observed fission events in the late 1930ies [17,18]. However, microscopic effects lead to deviations of up to 10 MeV from this simple picture. Although the total potential energy or binding energy of an actinide nuclide is about 1600 MeV the microscopic effects have an enormous influence on the fission process and nuclear stability. They are obtained by use of the Strutinsky shell-correction method [19,20]. First a single-particle potential based on the shape selected is generated. This is done separately for neutrons and protons. We solve for the single-particle levels and obtain a level spectrum for neutrons and protons. By use of the Strutinsky shell-correction method we obtain the neutron and proton shell corrections. To a high order they are independent of each other. The total potential energy is the sum of the macroscopic energy and the proton and neutron shell corrections. By repeating this for the five million shapes we obtain a five-dimensional (5D) potential-energy surface. The selected shapes include shapes from the ground state to shapes with very small necks near scission. We actually include all shapes that occur within the three-quadratic surface parameterization, which has 5 independent shape parameters: shape elongation, the spheroidal deformations of the two emerging fragments, a neck diameter, and a mass division between the two emerging fragments. The random walk is then performed on this 5D potential-energy surface.

2.2. Five-dimensional random walks $\longrightarrow Y(A)$

To calculate fission yields for a particular compound system, we perform random walks on the previously calculated potential-energy surface. We locate the starting point at the ground-state shape. We then apply the Metropolis algorithm. Randomly we pick a neighbor point (one out of 242 in this case). We then decide if to proceed to that point as discussed in Ref. [9]. This step-wise progression of the walk continues until a point near scission is reached; in our case the walk is terminated at neck radius 2.5 fm. The mass split, or equivalently, the volume split, is tabulated at that point. It is assumed the divisions of Z, N, and A are each proportional to the volume division. Therefore we obtain $Y(A)$, $Y(Z)$, and $Y(N)$ which by construction are proportional to each other. That further implies that the two fragment values of N/Z are identical to the value of N/Z of the fissioning system.

2.3. Six-dimensional random walks $\longrightarrow Y(Z, N)$

Since we aim to study asymmetry distributions versus Z and N we now need two asymmetry variables, namely Z and N, not the single volume variable (A). We need to perform random walks on a six-dimensional potential-energy surface with these two asymmetry variables and construct such a six-dimensional potential-energy surface. Therefore we first calculate the neutron shell corrections for volume asymmetric splits that correspond to the desired range of $N_1 : N_2$ (integer) splits. For each of these splits the other four shape variables are also varied, as usual, so again we obtain millions of the corresponding neutron shell corrections. Then, correspondingly, we calculate the proton shell corrections for the desired range of $Z_1 : Z_2$ (integer) splits and in addition we also save the macroscopic energy for these splits. To obtain the potential energy for a split $Z_1, N_1 : Z_2, N_2$ we add the two calculated proton and neutron shell corrections for the $Z_1 : Z_2$ and $N_1 : N_2$, respectively and furthermore add the stored macroscopic energy corresponding to the $Z_1 : Z_2$ split. This split corresponds to a $N_1 : N_2$ split ratio that is identical to the $Z_1 : Z_2$ ratio. Since we now study a different neutron split we must calculate how the macroscopic energy changes. It will be mainly the symmetry energy and Coulomb self energies that change. To obtain the relevant macroscopic energy difference compared to the stored one we calculate the total macroscopic energy for two separated spherical fragments corresponding to the Z and N asymmetry values for the stored macroscopic energy and then for the actual proton (same as the stored value) and neutron splits. The difference between these two macroscopic energies is added to the potential energy so the correct total macroscopic energy for the split $Z_1, N_1 : Z_2, N_2$ is obtained.

Thus, we have the required six-dimensional potential-energy surface on which we perform the random walks in a similar manner as in the five-dimensional case. We emphasize again that the asymmetry coordinates are now Z and N. An independent "mass asymmetry" coordinate does not exist in the 6D extension. However mass distributions $Y(A)$ can obviously be obtained by summing the yields $Y(Z, N)$ along lines of constant A. Full details, sensitivity studies and benchmarks are in Ref. [10]. This is the model we use here, whereas most previous studies with the BSM method used the version outlined in Sect. 2.2 [9,21–23,10,24].

3. Comparing fission theory and experiment

There are several challenges in comparing fission theory with fission experiment.

It may seem that a direct comparison of calculated and experimentally measured fission quantities is to compare various calculated and experimental fission-fragment properties such as fission-fragment mass distributions $Y(A)$. Calculations usually provide pre-neutron (pre-n) emission results. Pre-n fragment mass distributions can be obtained experimentally but the resolution is usually limited, with an uncertainty of several nucleons. However, in the experiment of Schmidt and collaborators [2] fission-fragment charge distributions $Y(Z)$ were measured with one-proton resolution and are not affected by post-scission neutron emission. A large-scale comparison between calculated and measured fission-fragment charge yields of 70 nuclei showed encouraging agreement between theory and experiment [21].

Recent progress in both experimental and theoretical fission studies allows better and new types of comparisons between experiment and theory. Experiments have now determined fission-fragment yields as functions of both Z and N with better than one-nucleon resolution, see Refs. [26,27]. These experimental advances and the theoretical developments [10] discussed above allow us to compare, for the first time, the calculated $< N > /Z$ variation with Z as well as isotopic distributions to experiment.

4. Calculated results

The starting point of our study is theoretical yields $Y(Z, N)$, which we can calculate for any fissioning nuclide at any specified excitation energy E^*. By appropriate summations of $Y(Z, N)$ one trivially obtains theoretical charge yields $Y(Z)$ and mass yields $Y(A)$. We first present some comparisons of those yields to experimental measurements. Then we further test the recently developed model for the isotopic yields $Y(Z, N)$ by looking at the evolution of the fission-fragment $< N > /Z$ ratio with charge number for which experimental data have recently become available [26,27]. We also study details of the isotopic yields for several proton numbers.
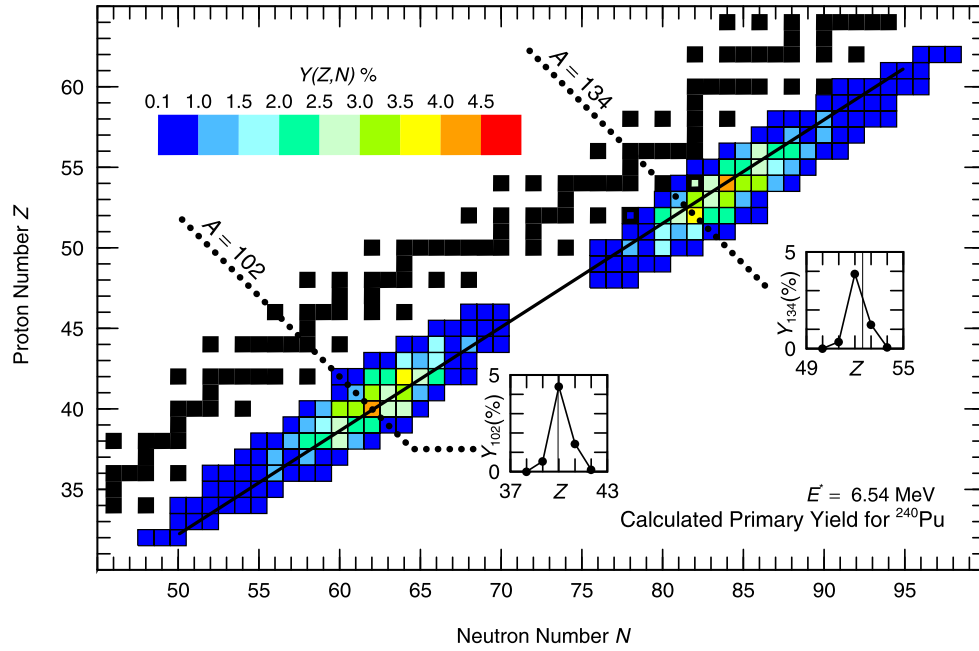
Fig. 1. Calculated fission-fragment pre-n yield $Y(Z, N)$. The black squares show β-stable nuclei; the solid black line gives the location of fission fragments if the $<N>/Z$ ratio in the fission fragments is assumed identical to the ratio in the fissioning parent nucleus, the so-called unchanged charge division (UCD) approximation. The two insets correspond to the isobaric yields along $A = 102$ and $A = 134$. The thin vertical lines correspond to the Z values of the black line at those A values, UCD assumption. Yields larger than 0.0001% are shown, while in the color chart area we only show yields larger than 0.1% to avoid distracting, large areas of blue.

4.1. Mass and charge yields

The most pronounced structure in the yield functions occurs at lower excitation energies [22]. We show in Fig. 1, in the form of a contour plot, the calculated pre-n isotopic yield $Y(Z, N)$ for the thermal neutron-induced fission reaction ^{239}Pu(n_{th},f), which corresponds to an excitation energy $E^* = 6.54$ MeV. In some earlier papers, for example [9,21,23,28], the charge yield was obtained as a simple transformation of the calculated yield $Y(A)$ based on the assumption that the fragment neutron-to-proton ratios were the same as in the fissioning compound nucleus. Under this assumption only fission fragments along the black line in the figure would be obtained, the so-called unchanged charge division (UCD) assumption. A recent study in Ref. [24] does provide yields $Y(Z, N)$ but it is also based on a calculation of $Y(A)$ along the black line in Fig. 1 by use of the methods described in Refs. [9,21,23,28]. The yields away from this line, along constant A are obtained by folding a Gaussian around the calculated $Y(A)$ value. This means that the yields along nuclides on any line parallel to the black line in Fig. 1 are just a scaled-down version of the calculated $Y(A)$. In our approach we observe that the calculated yields for constant A is not a Gaussian centered on the black line. In the lighter fragment region there is more yield on the neutron-deficient side of the black line whereas in the heavy region there is more yield on the neutron-rich side. This asymmetry assures that the proton and neutron numbers in the light fragment and its heavy partner sum up to those of the compound nucleus. At a specific A the yields deviate from a Gaussian about the black line, as is seen in the insets in Fig. 1, because we *calculate* the potential-energy landscape as a function of Z and N.

In Fig. 2 we show the calculated pre-n mass yield $Y(A)$ for ^{239}Pu(n_{th},f), obtained from the calculated isotopic yield $Y(Z, N)$ compared to experimental pre-n results from Ref. [25]. The calculated numbers, which are obtained for all integer values of A, have been folded with a Gaussian with $\sigma_r = 2.12$ u corresponding to the experimental resolution. The overall features of these experimental results are reproduced although localized differences remain.
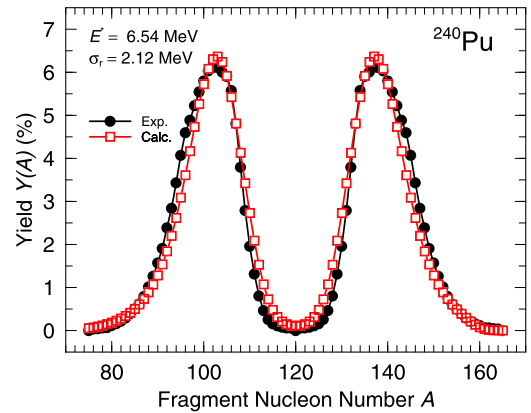

Fig. 2. Calculated ^{240}Pu fission-fragment mass distribution $Y(A)$ for thermal neutron-induced fission (^{239}Pu(n_{th},f)) compared to experiment [25]. The calculations have been folded with a Gaussian with $\sigma_r = 2.12$, to be consistent with the experimental resolution. The calculations and experiment are both pre-n.

To compare our calculated results for charge distributions to measurements we select the experimental data for ^{240}Pu fission at an average excitation energy $E^* = 10.7$ MeV from Ref. [27], since experimental charge yields are not available at thermal energies.[1] Our calculated charge distribution is obtained from summing up the calculated isotopic yield $Y(Z, N)$ at $E^* = 10$ MeV which we compare with the experiment in Fig. 3. The differences between experiment and calculations partly arise because of theoretical model uncertainties and partly because the calculations are carried out at 10 MeV but the experiment contains contributions from an 8 MeV range of energies with a mean at 10.7 MeV [29,30]. However the width of the experimental excitation energies do not noticeably affect the $<N>/Z$ curve [31] as we discuss in the next section.

---

[1] In Ref. [10] Fig. 7 the bottom panel shows the calculated charge yield in ^{240}Pu(n_{th},f) compared to an *evaluated* data base.
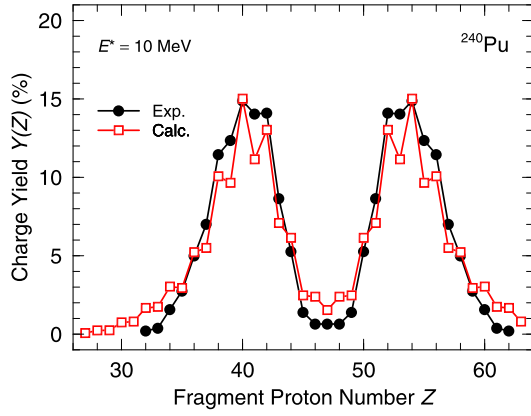
Fig. 3. Calculated ^{240}Pu fission-fragment charge yield $Y(Z)$ at $E^* = 10$ MeV compared to experiment [27]. The experiment has a better than one-proton resolution but the experimental excitation energy has some width around its average value, see text.
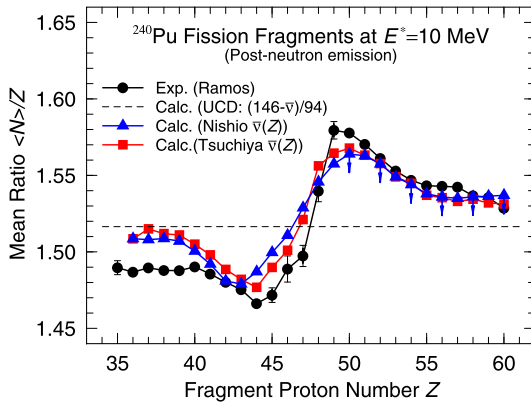

Fig. 4. Calculated fission-fragment average neutron-to-proton ratio $< N > /Z$ versus fragment charge division compared to experiment [30]. Both the calculated results and the experimental data are for post-n emission. The dashed line is obtained under the assumption the $< N > /Z$ ratio is the same in all fragments as in the fissioning compound system, but with the average number of emitted neutrons subtracted. The blue arrows indicate the possible effect of the variation with energy of the number of post-scission neutrons, see text for a discussion.

4.2. Variation of $< N > /Z$ with fragment charge

Recently the variation of the average $< N > /Z$ with fission-fragment charge number was measured in a number of fission reactions [26,30]. We compare our calculated results to the measured results for fission of ^{240}Pu at an average excitation energy of 10.7 MeV. These measured data are plotted as connected black solid dots in Fig. 4. We note that the experimental data correspond to a distribution in E^* with a finite width, while the calculation is performed at a single value $E^* = 10$ MeV, close to the average experimental value of 10.7 MeV. This is a reasonable approach as the detailed experimental analysis showed that the influence of E^* on the $< N > /Z$ curve is very small within the E^* range spanned in the measurement [31]. In this and subsequent figures (Figs. 4–9) the experimental data are post-n results. In ^{240}Pu fission at $E^* = 10$ MeV the average number of neutrons emitted per fission is about $\bar{\nu} = 3.45$ [32]. Assuming that the $< N > /Z$ ratio in the fragments is that of the compound nucleus (UCD assumption) minus the average number of emitted neutrons we obtain the result plotted as a dashed horizontal line in Fig. 4. We intend this line to be a "zero-order" reference, so that we obtain a clearer picture of the impact of the new features of our more detailed theory.

We use experimental data on neutron emission versus fragment mass number A to subtract from our pre-n results the average
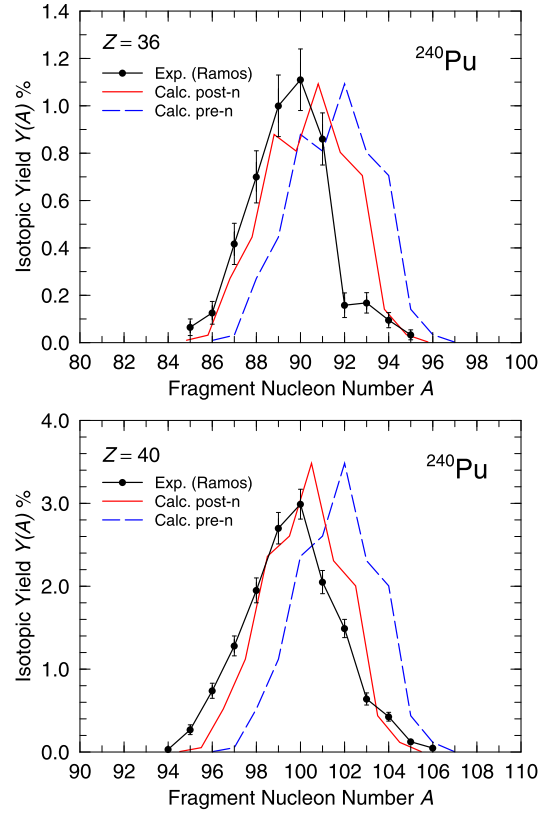

Fig. 5. Calculated pre- and post-n isotopic yields for krypton ($Z = 36$) and zirconium ($Z = 40$) compared to experiment [27].
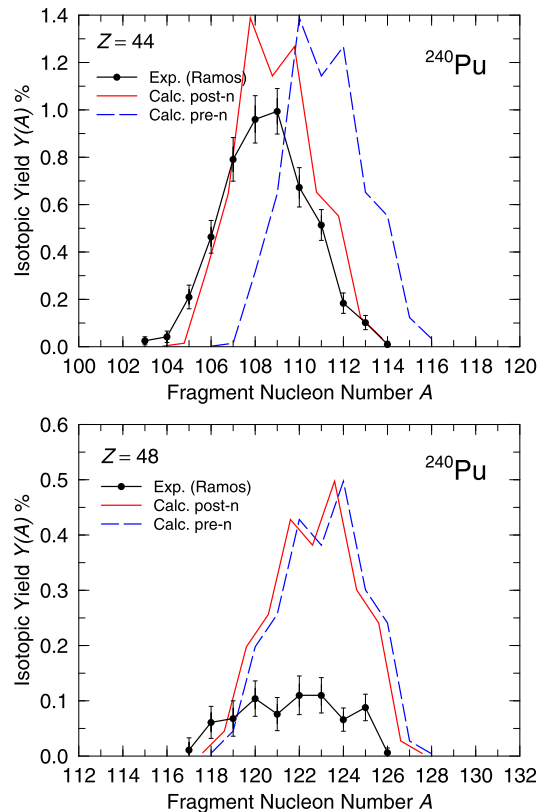

Fig. 6. Calculated pre- and post-n isotopic yields for ruthenium ($Z = 44$) and cadmium ($Z = 48$) compared to experiment [27].
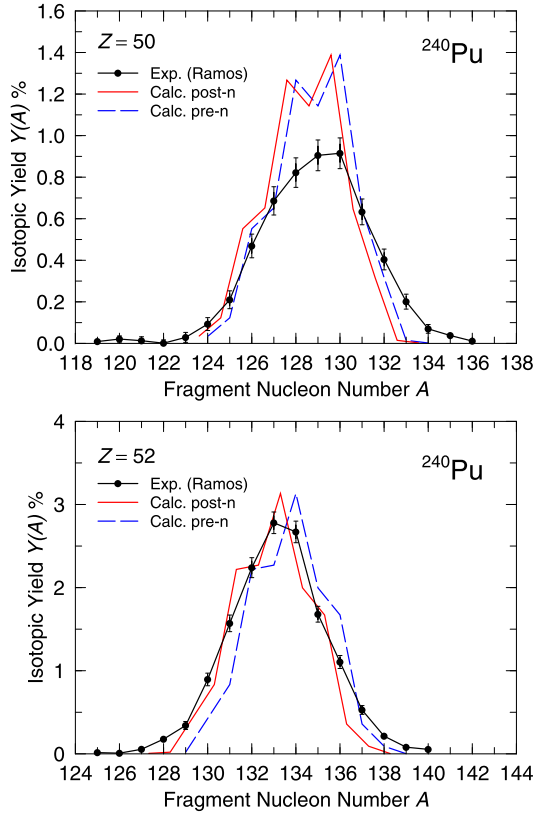
Fig. 7. Calculated pre- and post-n isotopic yields for tin ($Z = 50$) and technetium ($Z = 52$) compared to experiment [27].

Fig. 8. Calculated pre- and post-n isotopic yields for barium ($Z = 56$) and neodymium ($Z = 60$) compared to experiment [27].

number of neutrons emitted at each Z to obtain a post-n $< N > /Z$ curve. Thus it is partly "experimental" but since the main features of the curve still have their origins in the theoretical results it is a strategy that permits us to test the theoretical model for the isotopic yield $Y(Z, N)$. To illustrate some of the experimental uncertainty in this type of data we use results of two experiments, namely those Ref. [33] and Ref. [34]. There are several caveats to note:

1. The measured neutron-emission data is versus mass number A.
2. Energy difference between neutron-emission measurements, which are for thermal neutron-induced fission, and the $< N > /Z$ experimental data which are at $E^* = 10.7$ MeV. However, it is experimentally well-established that the sawtooth post-scission neutron-emission curve evolves with E^* in such a way that up to rather high E^* the post-scission neutron multiplicity remains the same for the light-fragment wing. Only the fragments from the heavy wing exhibit some increase in the post-scission neutron multiplicity with rising initial E^* [35]. This implies that in our post-n emission curve we underestimate somewhat the number of neutrons emitted by the heavy fragment. Therefore, the right half of the "theoretical" post-n $< N > /Z$ curve would be an upper limit. We have indicated with blue arrows an estimate of the influence of the possible underestimate of emitted neutrons. The left half is, on the contrary, expected to be accurately corrected for post-scission emitted neutrons at the actual energy.

Therefore in our calculations we proceed as follows. First we obtain $(< N > /Z)_{\text{pre}-n}$ from our calculated isotopic yield $Y(Z, N)$ at $E^* = 10$ MeV. For a specific Z for which we have obtained an average N we subtract from this average N the experimental value
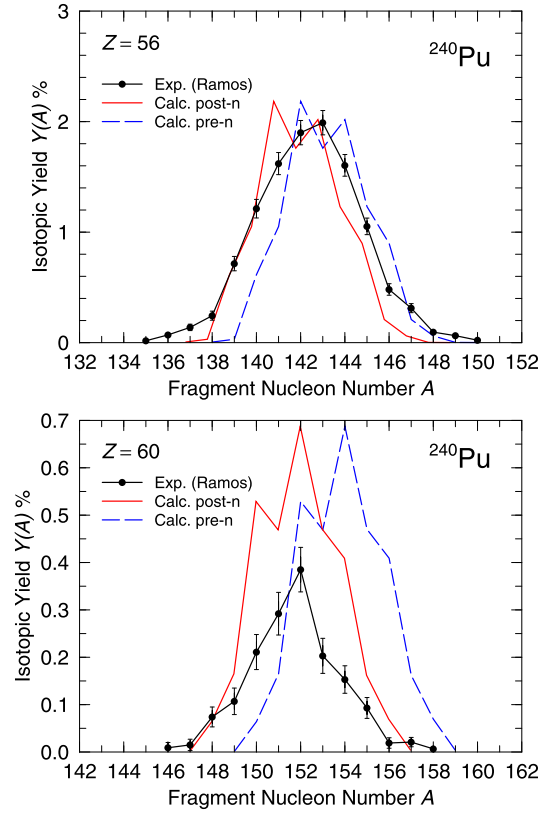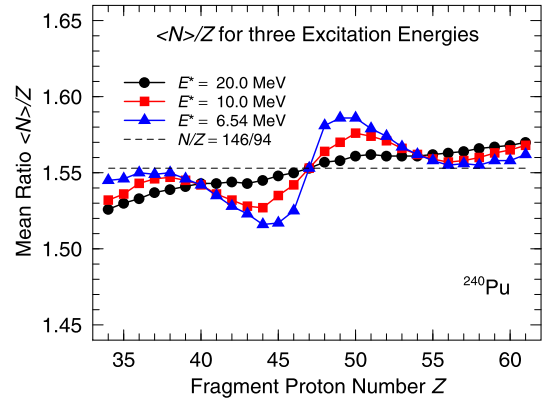

Fig. 9. Calculated fission-fragment average neutron to proton ratio $< N > /Z$ versus fragment charge division for increasing excitation energies. The dashed line is obtained under the assumption the $< N > /Z$ is the same as in the fissioning compound nucleus in all fragments. Results are before neutron emission.

for number of emitted neutrons $\bar{\nu}(Z)$ at $A_{\text{frag}} = (< N > /Z)_{\text{pre}-n} \times Z + Z$. The accuracy of the procedure to derive the theoretical post-neutron $< N > /Z$ as function of Z from the theoretical pre-n one and the experimentally available mass-dependent neutron multiplicities was investigated by means of GEF simulations, and estimated to be of the order of a few per mil in N/Z, i.e. ten times smaller than physical effect under study.

We show in Fig. 4 the calculated $< N > /Z$ results based on the two experimental data sets [33,34] for post-scission neutron emission. Our results explain the general features of the measured data, and in particular the strong change in the fragment $< N > /Z$ between $Z \approx 44$ and $Z \approx 50$. The calculation reproduces 80% of the steep "staircase rise" around symmetry ($Z = 47$). In terms

of rms deviations between experiment and calculations we find rms = 0.0358 with respect to the black, dashed line, rms = 0.0148 with respect to the curve marked with the square symbols with post-scission neutron emission based on the data in Ref. [33], and rms = 0.0138 with respect the curve marked with the triangular symbols, based on the data in Ref. [34]. We again note that the original BSM model as well as the prescription of Ref. [24] result in the dashed straight line. The extension to a full isotopic-yield model [10] therefore allows a more realistic modeling of a larger range of fission-fragment properties.

4.3. Isotopic yields

To further test the isotopic-yield model for $Y(Z, N)$ we display in Figs. 5, 6, 7, and 8 calculated isotopic yield distributions, which cannot be obtained within the original BSM model [9], for a number of representative isotopic chains, namely for $Z = 36$, 40, 44, 48, 50, 52, 56, and 60. Also displayed are experimental data from Ref. [27]. The calculated pre-n yield $Y(Z, N)$ results have again been corrected for post-scission neutron emission using experimental measurements, but in this case we only use one data set, namely that of Ref. [34]. There is encouraging agreement with the experimental data, except near symmetry (see $Z = 48$), and at $Z = 60$. Deviations near symmetry could already be anticipated from the Z yields of Fig. 3. A poor description of symmetric divisions is common to most current models. At present there is no consensus on its origin [36]. The discrepancy at the largest Z value, $Z = 60$, is very likely related to underestimated experimental yields [37] due to the difficulty in identifying heavy elements at Coulomb-barrier energies. However, we note that the mean value and shape of the $Z = 60$ distribution are reasonably described.

Because the correction $\bar{\nu}(Z)$ for neutron emission is the same for all isotopes of a specific proton number Z the calculated post-n isotopic distributions in Figs. 5–8 are identical to the pre-n ones except for a shift by an amount $\bar{\nu}(Z)$. Therefore the influence of post-scission evaporation in possibly altering the shape of the isotopic distribution is not accounted for. Besides a mere shift, neutron emission in general slightly broadens the distribution [38]. Also, the odd-even staggering is reduced relative to the staggering in the pre-n yields [38,12], which is not accounted for in the comparison in Figs. 5–8.

4.4. Variation of $< N > /Z$ with excitation energy

Finally, we show in Fig. 9, again for ^{240}Pu fission, the calculated pre-n $< N > /Z$ variation with proton number at three different energies, namely at $E^* = 6.54$ MeV, 10 MeV, and 20 MeV. There are no data for this full range of energies for $< N > /Z$ for ^{240}Pu. However, Fig. 10 in [30] shows experimental data for increasing energies for different nuclei.

Despite this limitation we note that the calculated behavior with increasing energy is consistent with the general trend with energy that is observed experimentally, namely that as the energy increases the structure in the $< N > /Z$ curve disappears, that is shell effects weaken. At the highest energy considered in Fig. 9 multi-chance fission may affect experimental results to some extent. However, the main trend is preserved, and at still higher energies the calculations would closely follow the slope given by the curve with the circular markers but with the undulations absent. This is also what is seen in experiment (see Fig. 10 in Ref. [30] and Fig. 3 in Ref. [39]). The increase of average neutron excess with charge number can therefore be understood in terms of the macroscopic model which shows that for β-stable nuclei $< N > /Z$ increases with increasing mass, or equivalently, charge number. This macroscopic-model property similarly affects the fission fragment $< N > /Z$ ratio dependence on Z.

5. Summary

We have compared calculated ^{240}Pu fission-fragment properties to experimental data. We focused on the fission-fragment isotopic composition. It is the first time this type of comparison between results of more fundamental theory (which has not been adjusted to the data compared to) and experimental data has been presented and is only made possible due to two recent advances. First, there are now available experimental fission-fragment isotopic yields with better than 1 u resolution [26,27]. Second, the theoretical model for fission-fragment mass yields based on folded-Yukawa potential-energy surfaces [7] and the BSM approach [9] has been generalized so that isotopic yields $Y(Z, N)$ can be calculated. In our comparison we find that the characteristic variation of $< N > /Z$ with proton number, in particular the strong fluctuation around symmetric division is clearly present in the calculated results, as is the evolution of $< N > /Z$ with energy. Also isotopic distributions are reasonably described.

Some of the differences between the calculated results and experimental measurements may arise because of the somewhat approximate treatment of neutron evaporation in the calculations. We also need to recall that all nuclear theories for heavy nuclei are "effective" theories so they are all of less than perfect accuracy. From nuclear mass calculations we know for example that the potential-energy model used here is accurate to about 0.6 MeV on average, somewhat larger for light nuclei which will contribute to the deviations seen in Fig. 4.

Declaration of competing interest

The authors declare that they have no known competing financial interests or personal relationships that could have appeared to influence the work reported in this paper.

Acknowledgements

References

[1] S. Steinhäuser, J. Benlliure, C. Böckstiegel, H.-G. Clerc, A. Heinz, A. Grewe, M. de Jong, A.R. Junghans, J. Müller, M. Pfützner, K.-H. Schmidt, Nucl. Phys. A 634 (1998) 89.

[2] K.-H. Schmidt, S. Steinhäuser, C. Böckstiegel, A. Grewe, A. Heinz, A.R. Junghans, J. Benlliure, H.-G. Clerc, M. de Jong, J. Müller, M. Pfützner, B. Voss, Nucl. Phys. A 665 (2000) 221.

[3] K.-H. Schmidt, J. Benlliure, A.R. Junghans, Nucl. Phys. A 693 (2001) 169.

[4] P. Möller, A. Iwamoto, in: Proc. Conf. on Nuclear Shapes and Motions. Symposium in Honor of Ray Nix, Sante Fe, NM, USA, Acta Phys. Hung., New Ser. 10 (1999) 241.

[5] P. Möller, A. Iwamoto, Phys. Rev. C 61 (2000) 047602.

[6] P. Möller, D.G. Madland, A.J. Sierk, A. Iwamoto, Nature 409 (2001) 785.

[7] P. Möller, A.J. Sierk, T. Ichikawa, A. Iwamoto, R. Bengtsson, H. Uhrenholt, S. Åberg, Phys. Rev. C 79 (2009) 064304.

[8] P. Möller, A.J. Sierk, T. Ichikawa, A. Iwamoto, M. Mumpower, Phys. Rev. C 91 (2015) 024310.

[9] J. Randrup, P. Möller, Phys. Rev. Lett. 106 (2011) 132503.

[10] P. Möller, T. Ichikawa, Eur. Phys. J. A 51 (2015) 173.

[11] K.-H. Schmidt, B. Jurado, Rep. Prog. Phys. 81 (2018) 106301.

[12] C. Schmitt, K.-H. Schmidt, B. Jurado, Phys. Rev. C 98 (2018) 044605.

[13] W. Nörenberg, Z. Phys. 197 (1966) 246.

[14] U. Quade, K. Rudolph, S. Skorka, P. Armbruster, H.-G. Clerc, W. Lang, M. Mutterer, C. Schmitt, J.P. Theobald, F. Gönnenwein, J. Pannicke, H. Schrader, G. Siegert, D. Engelhardt, Nucl. Phys. A 487 (1988) 1.

[15] M. Bolsterli, E.O. Fiset, J.R. Nix, J.L. Norton, Phys. Rev. C 5 (1972) 1050.

[16] H.J. Krappe, J.R. Nix, A.J. Sierk, Phys. Rev. C 20 (1979) 992.

[17] L. Meitner, O.R. Frisch, Nature 143 (1939) 239.

[18] N. Bohr, J.A. Wheeler, Phys. Rev. 56 (1939) 426.

[19] V.M. Strutinsky, Nucl. Phys. A 95 (1967) 420.

[20] V.M. Strutinsky, Nucl. Phys. A 122 (1968) 1.

[21] J. Randrup, P. Möller, Phys. Rev. C 88 (2013) 064606.

[22] P. Möller, J. Randrup, A. Iwamoto, T. Ichikawa, Phys. Rev. C 90 (2014) 014601.

[23] J. Randrup, P. Möller, A.J. Sierk, Phys. Rev. C 84 (2011) 034613.

[24] M.R. Mumpower, P. Jaffke, M. Verriere, J. Randrup, Phys. Rev. C 101 (2020) 054607.

[25] C. Wagemans, E. Allaert, A. Deruytter, R. Barthélémy, P. Schillebeeckx, Phys. Rev. C 30 (1984) 218.

[26] E. Pellereau, J. Taieb, A. Chatillon, H. Alvarez-Pol, L. Audouin, Y. Ayyad, G. Bélier, J. Benlliure, G. Boutoux, M. Caamaño, E. Casarejos, D. Cortina-Gil, A. Ebran, F. Farget, B. Fernández-Domínguez, T. Gorbinet, L. Grente, A. Heinz, H. Johansson, B. Jurado, A. Kelić-Heil, N. Kurz, B. Laurent, J.-F. Martin, C. Nociforo, C. Paradela, S. Pietri, J.L. Rodríguez-Sánchez, K.-H. Schmidt, H. Simon, L. Tassan-Got, J. Vargas, B. Voss, H. Weick, Phys. Rev. C 95 (2017) 054603.

[27] D. Ramos, M. Caamaño, F. Farget, C. Rodríguez-Tajes, L. Audouin, J. Benlliure, E. Casarejos, E. Clement, D. Cortina, O. Delaune, X. Derkx, A. Dijon, D. Doré, B. Fernández-Domínguez, G. de France, A. Heinz, B. Jacquot, A. Navin, C. Paradela, M. Rejmund, T. Roger, M.-D. Salsac, C. Schmitt, Phys. Rev. C 97 (2018) 054612.

[28] P. Möller, J. Randrup, Phys. Rev. C 91 (2015) 044316.

[29] C. Rodríguez-Tajes, F. Farget, X. Derkx, M. Caamaño, O. Delaune, K.-H. Schmidt, E. Clément, A. Dijon, A. Heinz, T. Roger, L. Audouin, J. Benlliure, E. Casarejos, D. Cortina, D. Doré, B. Fernández-Domínguez, B. Jacquot, B. Jurado, A. Navin, C. Paradela, D. Ramos, P. Romain, M.D. Salsac, C. Schmitt, Phys. Rev. C 89 (2014) 024614.

[30] D. Ramos, M. Caamaño, F. Farget, C. Rodríguez-Tajes, L. Audouin, J. Benlliure, E. Casarejos, E. Clement, D. Cortina, O. Delaune, X. Derkx, A. Dijon, D. Doré, B. Fernández-Domínguez, G. de France, A. Heinz, B. Jacquot, C. Paradela, M. Rejmund, T. Roger, M.-D. Salsac, C. Schmitt, Phys. Rev. C 99 (2019) 024615.

[31] D. Ramos, C. Rodríguez-Tajes, M. Caamaño, F. Farget, L. Audouin, J. Benlliure, E. Casarejos, E. Clement, D. Cortina, O. Delaune, X. Derkx, A. Dijon, D. Doré, B. Fernández-Domínguez, G. de France, A. Heinz, B. Jacquot, A. Navin, C. Paradela, M. Rejmund, T. Roger, M.-D. Salsac, C. Schmitt, EPJ Web Conf. 146 (2017) 04019.

[32] M.B. Chadwick, P. Obložinský, M. Herman, N.M. Greene, R.D. McKnight, D.L. Smith, P.G. Young, R.E. MacFarlane, G.M. Hale, R.C. Haight, S. Frankle, A.C. Kahler, T. Kawano, R.C. Little, D.G. Madland, P. Möller, R. Mosteller, P. Page, P. Talou, H. Trellue, M. White, W.B. Wilson, R. Arcilla, C.L. Dunford, S.F. Mughabghab, B. Pritychenko, D. Rochman, A.A. Sonzogni, C. Lubitz, T.H. Trumbull, J. Weinman, D. Brown, D.E. Cullen, D. Heinrichs, D. McNabb, H. Derrien, M. Dunn, N.M. Larson, L.C. Leal, A.D. Carlson, R.C. Block, B. Briggs, E. Cheng, H. Huria, K. Kozier, A. Courcelle, V. Pronyaev, S.C. van der Marck, CSEWG Collaboration, Nucl. Data Sheets 107 (2006) 2931.

[33] K. Nishio, Y. Nakagome, I. Kanno, I. Kimura, J. Nucl. Sci. Technol. 32 (1995) 404.

[34] C. Tsuchiya, Y. Nakagome, H. Yamana, H. Moriyama, K. Nishio, I. Kanno, K. Shin, I. Kimura, J. Nucl. Sci. Technol. 37 (2000) 941.

[35] A.A. Naqvi, F. Käppeler, F. Dickmann, R. Müller, Phys. Rev. C 34 (1986) 218.

[36] A.J. Sierk, Phys. Rev. C 96 (2017) 034603.

[37] D. Ramos, Priv. Comm., 2020.

[38] A.N. Andreyev, K. Nishio, K-H. Schmidt, Rep. Prog. Phys. 81 (2018) 016301.

[39] M. Caamaño, O. Delaune, F. Farget, X. Derkx, K.-H. Schmidt, L. Audouin, C.-O. Bacri, G. Barreau, J. Benlliure, E. Casarejos, A. Chbihi, B. Fernández-Domínguez, L. Gaudefroy, C. Golabek, B. Jurado, A. Lemasson, A. Navin, M. Rejmund, T. Roger, A. Shrivastava, C. Schmitt, Phys. Rev. C 88 (2013) 024605.

[40] P. Jaffke, P. Möller, P. Talou, A.J. Sierk, Phys. Rev. C 97 (2018) 034608.